Mapping nanoscale dynamic properties of suspended and supported multi-layer graphene membranes via contact resonance and ultrasonic scanning probe microscopies

Marta Mucientes[1*], Robert McNair[2], Adrian Peasey[2], Shouqi Shao[2], Joshua Wengraf[2], Kunal Lulla[1], Benjamin J. Robinson[1,3] and Oleg Kolosov[1,3**].

[1]Physics Department, Lancaster University, Lancaster LA1 4YB, UK

[2]Graphene NowNANO CDT, School of Physics and Astronomy, The University of Manchester, Manchester, M13 9PL, UK

[3]Materials Science Institute, Lancaster University, Lancaster LA1 4YW, UK

Email: *m.sanjuanmucientes@lancaster.ac.uk, **o.kolosov@lancaster.ac.uk,

ABSTRACT. Graphene's (GR) remarkable mechanical and electrical properties - such as its Young's modulus, low mass per unit area, natural atomic flatness and electrical conductance - would make it an ideal material for micro and nanoelectromechanical systems (MEMS and NEMS). However, the difficulty of attaching GR to supports, coupled with naturally occurring internal defects in a few layer GR can significantly adversely affect the performance of such devices. Here, we have used a combined contact resonance atomic force microscopy (CR-AFM) and ultrasonic force microscopy (UFM) approach to characterise and map with nanoscale spatial resolution GR membrane properties inaccessible to most conventional scanning probe characterisation techniques. Using a multi-layer GR plate (membrane) suspended over a round hole, we show that this combined approach allows access to the mechanical properties, internal structure and attachment geometry of the membrane providing information about both the supported and suspended regions of the system. We show that UFM allows the precise geometrical position of the supported membrane-substrate contact to be located and provides an indication of the local variation of its quality in the contact areas. At the same time, we show that by mapping the position sensitive frequency and phase response of CR-AFM response, one can reliably quantify the membrane stiffness, and image the defects in the suspended area of the membrane. The phase and amplitude of experimental CR-AFM measurements show excellent agreement with an analytical model accounting for the resonance of the combined CR-AFM probe-membrane system. The combination of UFM and CR-AFM provide a beneficial combination for the investigation of few-layer NEMS systems based on two dimensional materials.

1. Introduction

Graphene (GR) and other two-dimensional materials (2DM's) have drawn extensive interests thanks to their remarkable structures and exceptional mechanical, electrical, thermal and optical properties. GR in particular holds significant potential for micro and nanoelectromechanical systems (MEMS and NEMS) applications, transparent and flexible electrodes, optical modulators and nanomechanical resonators operating in classical and quantum regimes [1-5]. However, there are several major challenges for such devices; particularly important for NEMS applications, is the quality of the 2DM-substrate contact, effects of inhomogeneous in-plane stresses [6] and, for the few-layer and heterostructured 2DM's, interlayer defects. To investigate and mitigate these, one needs matching nanoscale characterisation methods, with the ability to map nanomechanical properties, sensitivity to the stresses in the suspended areas, and the capability to evaluate the quality of the interfacial contact. While commercially available atomic force microscopy (AFM) [7-11] and optical detection methods [12] have been commonly used to study suspended 2D materials, the material-substrate interaction and nanomechanical mapping across the whole NEMS structure remains challenging with limited reports in this area [13-15]. One promising technique is contact resonance AFM (CR-AFM) which has been shown to be able to detect subsurface holes under the 2DM's membrane[16-18] and to measure the local stiffness of the structure [18, 19]. At the same time, these studies indicated that the observed shape of the 2DM structure and recorded amplitudes varied significantly depending on the CR-AFM operation frequency, requiring independent methods to determine the geometry of such 2DM's "nano-drum". Here we combine AFM with ultrasonic excitation, ultrasonic force microscopy (UFM), and a phase sensitive variable frequency CR-AFM, to effectively observe the quality of the interface of the "supported" graphene and the substrate, to obtain nanomechanical maps of the suspended GR nanodrum structures and to provide quantitative comparison of the nanomechanical images and theoretical models.

2. Experimental details

The multi-layer graphene (MLG) nanodrums were produced via transfer of mechanically exfoliated MLG on top of a Si/SiO_2 substrate with 300 nm thermal oxide on the top. The substrate was pre-patterned with circular holes with a diameter of 1.9 μm etched to the depth of 150 nm in SiO2 layer *via* optical lithography and CHF_3/Ar reactive ion etching (see supplementary materials, SM, for the details). For the GR exfoliation [20], we used Gel-Pak® PF-4X film (0.5 mm thickness), with the resulting flakes transferred directly to the substrate. The substrate was treated in 98% Ar/2% O_2 plasma (PlasmaPrep2, Gala Instruments) for 10 min immediately prior to the transfer, to remove organic contamination and increase the adhesion of the graphene to the substrate.

The UFM and CR-AFM measurement setup was implemented by modifying a commercial AFM (MultiMode with Nanoscope-VIII controller, Bruker, Santa Barbara, USA). In both modes the out-of-plane vibration of the sample was realised by attaching it to a high frequency piezoceramic transducer (PI, Germany) *via* crystalline salol [21], with the transducer excited by a 33220A signal generator (Keysight, USA) (figure 1(a)). The resulting cantilever deflection signal was acquired using a custom-made signal access box with low noise high frequency signal buffers. In CR-AFM mode, the amplitude and phase of the AFM cantilever deflection at the excitation frequency in the range 10-100 kHz was detected by the lock-in amplifier (SRS-830, Stanford Research Systems, USA). In the UFM mode, the sample vibration was excited at the carrier frequency f_{UFM} in the range 4 to 5 MHz and is amplitude modulated using a triangular waveform at frequencies f_{mod} between 1-5 kHz. In this mode, the lock-in amplifier was detecting the amplitude of the deflection at the modulation frequency f_{mod}. As previously reported [21], the UFM signal at the modulation frequency is the result of nonlinear force-vs-distance dependence of the force interaction between the probe tip and the sample, reflecting the local stiffness of the material under the AFM tip. In a qualitative explanation, stiffer areas of the sample have a higher slope of force-vs-distance dependence, resulting in a more efficient "rectification" of the HF signal and hence a higher UFM signal. More detailed quantitative explanation of UFM sensitivity is given in [22]. With the range of effective Young's moduli ranging from 5 to 80 GPa (see e.g. table II in [21]), one would expect that UFM will be fully sensitive to the graphene layers on the substrate [23].

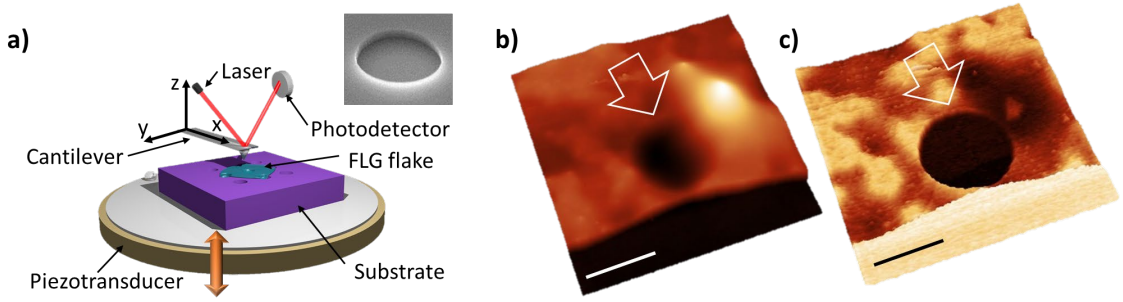

Figure 1. (a) Schematics of experimental setup for UFM and CR-AFM measurements, inset – SEM image of the hole in SiO2/Si substrate defined by optical lithography. (b) 3D rendering of contact AFM topography and (c) UFM nanomechanical image of the multilayer GR flake of 12 nm thickness over the hole in the substrate (f_{UFM} =4.2 MHz). Scale bars 1.5 um.

In both modes, a commercial contact AFM probe (ContAl-G, Budget Sensors) cantilever with the nominal 10 nm tip radius of curvature was used. The spring constant of the cantilever was measured using "Sader method" [24] to provide k_c = 0.184 N m^{-1}, matching the data obtained by the thermal

calibration method implemented by the AFM manufacturer (Bruker). In CR-AFM mode, the cantilever is brought into contact with the stiff material (SiO_2/Si substrate) resulting in an increase in the free cantilever resonance frequency of f_0=13 kHz to contact resonance frequency $f_{CR\text{-}R}$ = 64.6 kHz (in the contact with the substrate in the absence of lateral scanning). In order to find this contact resonance frequency we performed frequency sweeps obtaining the maximum amplitude of the oscillatory deflection signal.

3. Results and discussion

Both UFM and CR-AFM use dynamic approaches for mapping the mechanical properties of the GR membrane; hence, the first question is, what membrane properties are measured? First, we estimate the resonance frequencies of mechanical resonators based on suspended MLG flakes; these depend on GR Young's Modulus, E_s; Poisson's ratio, v_s; density, ρ_s; pre-tension, T, as well as the flake thickness, t, and the radius of the suspended area, R. For the resonators made by graphene monolayer the tension usually dominates as their bending rigidity is insignificant comparing with one produced by the tension [6, 7, 12]. However, for the resonator based on thicker MLG flakes, the minimal resonance frequency at zero tension is determined by the circular plate behaviour, with tension further increasing this frequency. For the plate the fundamental resonance frequency is given by the equation [25]

$$f_p = \frac{10.21}{4\pi}\sqrt{\frac{E_s}{3\rho_s(1-{\nu_s}^2)}}\frac{t}{R^2} \qquad (1)$$

For MLG flake with the dimensions presented in figures 1 and 2, the fundamental resonance frequency is f_p~138 MHz. This is several orders or magnitude higher than the frequencies of both CR-AFM (10-100 kHz) and UFM (4-5 MHz), used in our experiments, and therefore we can considere the GR membrane as a spring, neglecting its mass, allowing to use the formalism reported elsewhere [26-28] to describe the dynamics of the cantilever terminated with the spring. As we see later in the theoretical analysis section, the cantilever-sample system can be modelled as a cantilever supported at the free end by a spring, with respective k_c and k_s cantilever and sample stiffness, $k_s = dF/dz$ where F is the force experienced by the cantilever and z is the deflection of the plate from the equilibrium measured at the point of contact [29, 30]. Therefore, as a good approximation, we can consider that both UFM and CR-AFM are measuring a local stiffness of the membrane. With UFM being essentially an off-resonance method known to monotonously map the stiffness to the amplitude to the signal

[21], the CR-AFM due to its resonance nature [17, 18] provides more complicated response that we first investigate experimentally and then theoretically analyse comparing these studies.

The combination of AFM and high frequency excitation increases the sensitivity of the measurement setup to the mechanical properties compared to the standard force-distance spectroscopy and its option Peak Force^{TM}. These allowed mapping of the entire sample area, with true nanoscale spatial resolution and, in the case of UFM, eliminating friction [31] providing a non-destructive approach especially valuable when the supported sample is investigated. Figure 1 b, c) shows a typical topography and UFM images of the GR flake spanning the hole in the Si/SiO2 substrate (inset in figure 1a), with the UFM image showing a well-defined hole in the supported area. Figure 2 compares topography, UFM and CR-AFM modes for this flake. CR-AFM uses the resonance frequency of the cantilever in contact with the sample while scanning across the sample, to quantify the sample contact stiffness, k_s using analytical approaches described elsewhere [26, 32]. In both methods the k_s is probed by the AFM cantilever that can be in the minimal approximation represented as a spring k_c and effective mass m^* as schematically illustrated in the figure 2 c) with changes in k_s affecting the measured amplitude (UFM) or a frequency dependent response (CR-AFM). The detailed analysis of this measurement in application to the GR flake is presented in the theoretical part of this section. Figure 2(a) shows the topography of the test sample with the 12 nm MLG flake deposited over the hole. In the topography image, the hole β is barely observed as the smooth depression on the surface of MLG (arrow). The UFM nanomechanical image figure 2(b) clearly delineates the boundary of the hole corresponding to the edge between the lower stiffness (denoted by **L** in the figure 2 f) suspended region β and supported area α of higher stiffness (**H**, figure 2 f) enabling high precision measurements of the geometry of the membrane boundary (radius R=940± 5 nm in this structure). UFM also reveals neighbouring defects γ and γ' that show in the topography image as bulges of variable height, resulting in the weaker MLG – substrate interaction and interfacial defects and reducing contact stiffness (darker contrast in figure 2(b)), with the similar contrast to delaminations reported elsewhere [33]. It is interesting to note that the defects that has the internal particle show in UFM with the bright (higher stiffness) area inside the defect (γ') while defects without such particle (γ) have uniform low stiffness, as schematically illustrated in the figure 2 i). While UFM has superior contrast to the high stiffness (supported) areas of GR nanostructures, it is not sensitive to the variations of the contact stiffness within the suspended membrane area, which in this case is below the UFM sensitivity range of 10^2 to 10^5 N m^{-1} [22, 34]. It should be noted, though, that for 2D membranes of smaller dimensions and/or larger thickness, the UFM may become directly sensitive to the properties of the suspended areas as well as seen from the ψ and γ'. In the case of our nanostructure, to map and quantify its stiffness, we used CR-AFM that provided an excellent mechanical contrast in the suspended areas. Figure 2 panels

(d,e,g,h,j,k) shows a set of the CR-AFM amplitude and phase images obtained by detection of amplitude and phase of the cantilever deflection at the different sample excitation frequencies f_{CR} [35]. For reference, the topography and UFM image of the same area are provided in the panels (a) and (b). While CR-AFM demonstrates excellent contrast to the suspended area of the membrane and to the supported areas of the MLG, one can see that both the contrast, shape, and dimensions of the membrane are varied significantly depending on the frequency used.

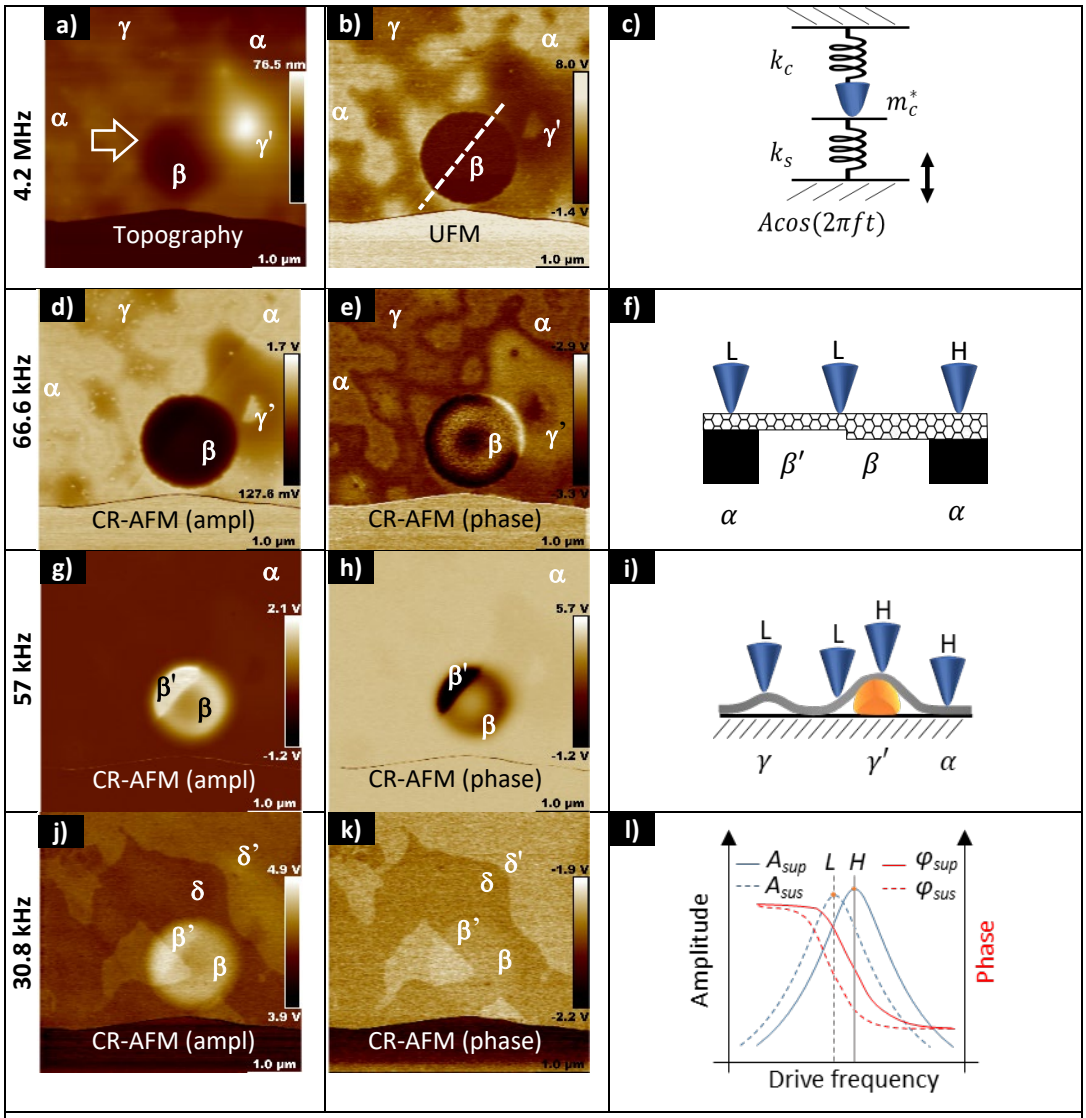

Figure 2. (a) AFM topography and (b) UFM map of the 12 nm thick MLG flake on the substrate with the hole (arrow) with *R*=940 nm. (d,e,g,h,j,k) Set of the CR-AFM amplitude and phase maps of the same area (d-e) at 30.8 kHz, (g-h) 57.0 kHz, and (j-k) 66.6 kHz. Greek letters show different features of the structure: α - supported GR membrane, β, β' –suspended membrane areas above the hole, γ, γ' - delaminated or weakly supported areas, δ, δ' – areas of contrast potentially linked with the subsurface defects in the membrane, c, f, i, l) schematics of the nanomechanical features observed in the CR-AFM and UFM: c) simplified diagramme of the interaction of dynamic AFM and the sample, f) expected nanomechanical contrast in the α, β and β' areas around the hole, **H** and **L** denoting high and low stiffess, respectively, i) schematics of the nanomechanical contrast in γ and γ' features, and l) diagram explaining expected amplitude and phase of CR-AFM response in the area of high (H) and low (L) stiffness in supported and suspended areas, respectively, detailed description in the text.

In figure 2 we compare three sets of the CR-AFM phase and amplitude response for the excitation frequency around the tip-substrate contact resonance frequency ($f_{CR\text{-}R}$=64.6 kHz).

A CR-AFM image at f_{CR}=66.6 kHz (figure 2(d,e)) shows the hole (β) as a uniformly dark area surrounded by the bright (high amplitude) substrate (β), as would be expected as frequency corresponds to the resonance of the cantilever-tip in contact with the substrate. The hole is similar to the UFM image in size, whereas the phase is presented as a concentric bright halo around the darker hole. The amplitude images are generally similar to ones reported by Ma et al [16] including the area of the delaminations γ and γ' as they affect the resonance conditions, whereas phase images that show variations similar to the UFM image, although with opposite contrast, require more detailed analysis. At lower frequency f_{CR}=57.0 kHz (figure 2 g,h) both amplitude and phase CR-AFM clearly shows the similar donut-shaped hole, with lower stiffness of the GR membrane in the suspended areas β, suggests lower resonance frequency, that explains the generally brighter contrast of these areas at the lower excitation frequency as indicated in figure 2 l). Surprisingly, the apparent diameter of the hole is now reduced diameter with a clear β' segment (bright in the amplitude and dark in the phase image) running at 45° across the hole. Given absence of the linked topographical features on the surface of the membrane, that is likely to be attributed to the change of the membrane thickness at the back side of the membrane in the β' area. Interesting that amplitude CR-AFM image in the figure 2 d) indicates a faint line across the hole coinciding with the β-β' boundary. Finally, the f_{dr}=30.8 kHz amplitude image (figure 2 j)) shows the hole as a donut-shaped bright area with a darker central area (β), whereas the phase image (figure 2 k)) has practically no contrast to the hole. At the same time, both amplitude and phase images clearly show the internal structure of the membrane (δ, δ') not visualised in the topography, UFM or CR-AFM at other frequencies. Given the shape of the features and the absence of the contrast in the topographical image (sensitive to the surface features) and in UFM (that would be most sensitive to sample – interface contact [13]) these might be interpreted as internal cracks ore extra planes in the MLG flake which induces a change in the stiffness of this particular area, possibly accounting for shear forces contribution to the CR-AFM signal. Overall, while the rich contrast obtained in CR-AFM for such GR nanostructure is outstanding, and the ability to observe subsurface features corresponds to the one reported by the variable frequency AFM imaging of cellulose fibres [36], the strong qualitative and quantitative dependence of the contrast on the excitation frequency requires more detailed experimental studies and matching analysis to help with the interpretation of the CR-AFM data.

In order to consistently analyse the frequency dependent response of CR-AFM, we obtained a set of one dimensional scans – profiles along the single line shown in figure 2(b), while changing the frequency in 1 kHz steps from 50 to 69 kHz that includes the reference, f_{CR}, (stiff sample). By continuing

acquisition of the amplitude and phase signal, we collected the two-dimensional amplitude and phase – vs position/ frequency graphs, correspondingly, $A(r, f_{dr})$ and $A(\phi, f_{dr})$, as shown in figure 3 where the horizontal axis is the position of the probe across the hole, r, and vertical – the driving frequency f_{dr}, whereas the brightness corresponds to the amplitude or phase of the CR-AFM.

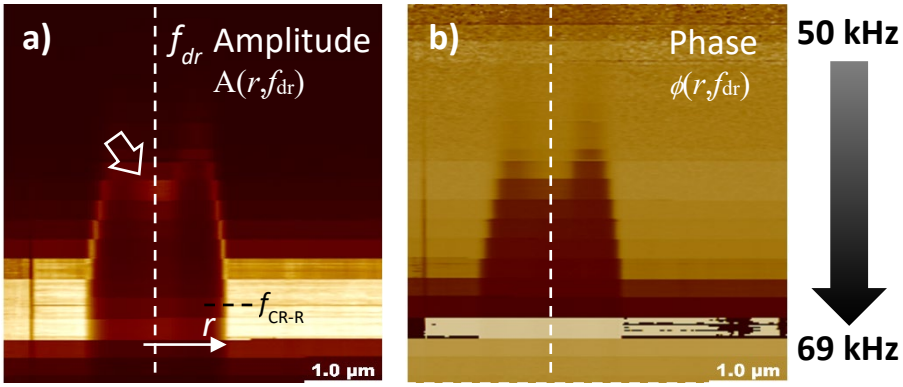

Figure 3. Plot of the CR-AFM response as the function of the position r across the hole (horizontal axis, r) and frequency (vertical axis, f_{dr}) with (a) amplitude A as the function of $A(r,f_{dr})$ and (b) $\phi(r,f_{dr})$ phase profile at driving frequency f_{dr} changing from 50 to 69 kHz in 1 kHz steps.

As we can see, the apparent "diameter" of the hole as seen by the CR-AFM is varied from the largest at $f_{dr} = f_{CR-R}$ to significantly reduced at lower driving frequencies ($f_{dr} < f_{CR-R}$). Also, the second maximum (arrow in the figure 3(a)) that would create a "ring" in the x-y image, appeared in the amplitude CR-AFM at the frequencies $f_{dr} < f_{CR\text{-}R}$. These phenomena can be qualitatively explained by the changing of contact stiffness of the tip-membrane contact that is the lowest in the centre and the largest at the periphery approaching "infinite" stiffness for the supported MLG layer. It is known that the resonance frequency of the cantilever-tip in contact with the membrane decreases with the decrease of its stiffness [26, 32]. Therefore the condition for the resonance for the decreased driving frequency f_{CR} are satisfied in the more central area of the membrane away from its border, resulting in the smaller diameter of the membrane, creating a bright ring at the position where the resonance occurs. In order to better understand and quantify our observations, we have used the analytical and modelling approach described below.

The equation of the dynamic deflection of the cantilever is given as $\frac{\partial^2 z}{\partial t^2} + \frac{E_c h^2}{12\rho_c}\frac{\partial^4 z}{\partial x^4} = 0$ where E_c is the Young's Modulus, ρ_c is the density, h is the thickness of the cantilever and x-z are the coordinates according the sketch in the figure 1(a). With density and Young's modulus of Si known, the length of the cantilever can be easily determined, by the optical microscope image, allowing to use Sader method providing cantilever stiffness k_c = 0.184±0.008 N m^{-1} that allows us to estimate the thickness of the cantilever h = 5.86 10^{-7} m. We can then calculate the resonance frequency of the

cantilever in the contact with the samples of varied sample stiffness k_s (see SM section SM3 for the derivation of this dependence). By substituting the values for the free cantilever, $k_s \rightarrow 0$, and experimentally obtained resonance frequency: f_0=13.8 kHz and the experimentally obtained CR-AFM frequency for the Si/SiO2 substrate that can be presented as infinitely stiff for the fundamental mode of the contact resonance [26], $k_s \rightarrow \infty$, in the substrate area of $f_{CR\text{-}R}$ = 64.6kHz, we obtain the CR-AFM response curve in figure 4. This curve 4 relates the resonant frequency of the cantilever with the ratio between the stiffness of the sample and the cantilever (k_c/k_s). We used high precision measurements of contact stiffness using a force modulation approach. It uses a ratio of the low frequency (2.7 kHz) quasi-static response of AFM in supported and suspended areas as described elsewhere [11]. Using this, we found that the stiffness of the sample in the centre of the membrane to be k_s = 2.15±0.008 N m^{-1}. By substituting this value in the equations in the SM section SM3 (graphically represented in Figure 4), we expect the resonance in the centre of the membrane to be around 45 kHz that corresponds well to the images in Figure 2, showing a brighter contrast of the membrane central area.

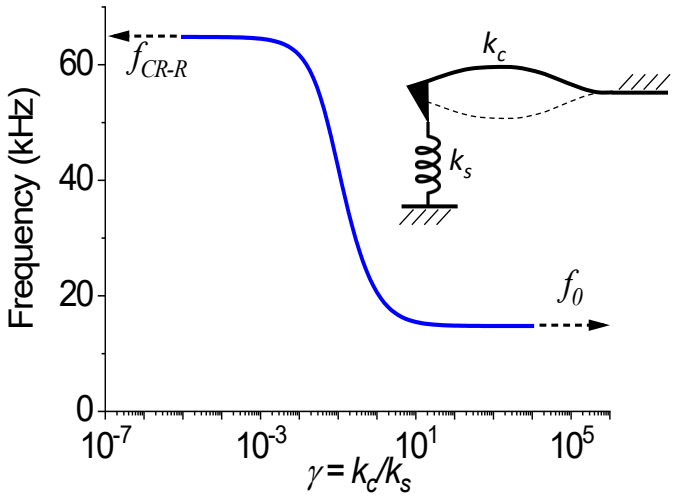

Figure 4. Resonant frequency for the CR-AFM f_{CR} for the first contact resonance mode (n=1) as a function of the cantilever-sample stiffness ration k_c/k_s.

In the case of a circular plate, the stiffness of the sample probed by the AFM tip depends on the distance from the centre of the plate to the contact point, as well as on the boundary conditions at the edge of the MLG flake. It is useful to estimate the possibility of shear stresses occurring during the CR-AFM measurement affecting the measurements and hence, data interpretation. We therefore calculated the maximal shear stresses in the MLG plate using final elements analysis (see SI, section 4 and Figure S1). We found that the maximal shear stress in all direction was below 1.5×10^7 N m^{-2} for

the typical maximal force applied to the AFM tip of 50 nN. These values are an order of magnitude smaller than typical shear strength between GR layers required for the sliding of 1.5-1.8×10^8 N m^{-2} [37, 38]. Given that the modulation of the shear stress is at most 10% of the permanent shear stress, we conclude that interlayer sliding should not occur in the AFM measurements confirming considerations elsewhere [7, 8, 39].

For the circular plate the two typical boundary conditions are – a) simply supported at the single circular line around the hole rim resulting in no bending moment applied to the plate at the edges (figure 5(a)) and b) - clamped when the edges of the plate are forced to be kept parallel to edges of the substrate surface (figure 5(b)). In the first case, the distribution of the stiffness as a function of radius *r* from the centre of the plate is given by [40]

$$k_s(r) = \frac{1}{H(r)c_0 a^3} \tag{2}$$

where *a* is the radius of the plate and *H(r)*, b_0 and c_0 expressed as

$$H(r) = \frac{1}{\pi D a^4}\frac{2(1+\nu_s)}{9(5+\nu_s)}(r^3 - b_0 a r^2 + c_0 a^3); \qquad b_0 = \frac{3(2+\nu_s)}{2(1+\nu_s)}; \qquad c_0 = \frac{4+\nu_s}{2(1+\nu_s)} \tag{3}$$

with the bending stiffness *D* defined as $D = \frac{E_s t^3}{12(1-\nu_s{}^3)}$.

In case of MLG flake clamped in the edges (figure 5(b)), the reference [40] provides stiffness distribution governed by the following equation

$$k_s(r) = \frac{16\pi D a^2}{(a^2 - r^2)^2} \tag{4}$$

In the centre of the plate the stiffness is then expressed as $k_s(r=0) = 16\pi D/a^2$. By substituting the parameters of the flake into the equation and using the in-plane Young's modulus of graphene of 1 TPa [41], we obtain the calculated value of the stiffness in the centre of the plate of k_s = 5.94 N m^{-1}, that is more than twice the experimental one, k_s = 2.15±0.008 N m^{-1} measured using the force modulation method explained above. At the same time, for the simply supported plate, the stiffness in the centre will be expressed as

$$k_s(r=0) = \frac{9\pi D(5+\nu_s)}{2{c_0}^2 a^2(1+\nu_s)} \tag{5}$$

resulting in calculated $k_s(r=0)$=2.35 N m^{-1}. We can therefore conclude that the simply supported model has better fit with the experimental results.

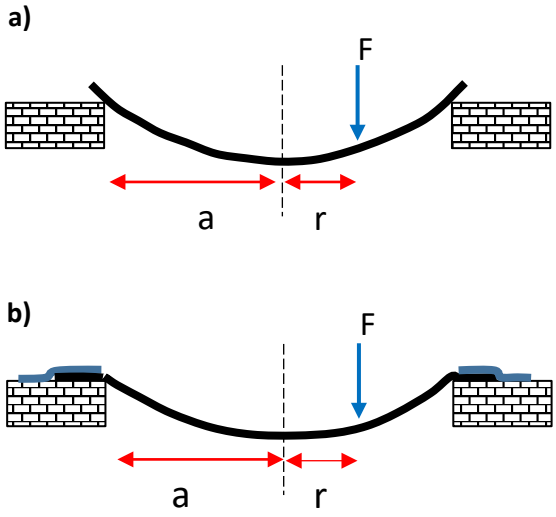

Figure 5. Two typical boundary conditions for the plate suspended over circular hole – (a) simply supported edges and (b) clamped edges.

The equations 2 and 3 together with the relation presented in the figure 4 (with the corresponding equations in SI) allow to link the resonant frequency f_{CR} and the stiffness of the membrane with the spatial position (the radius from the centre where the probe is located) where the maximum amplitude is located. We can further extend this analysis by considering the amplitude and phase of a cantilever as driven damped simple harmonic oscillator with the resonance frequency calculated by the approach defined above. In this case, the amplitude A and phase φ of the response of the cantilever are expressed as

$$A = \frac{A_0[\omega_{CR}(r)]^2}{\sqrt{([\omega_{CR}(r)]^2 - \omega_{dr}^2)^2 + \frac{\omega_{dr}^2}{[\omega_{CR}(r)]^2 Q}}}; \qquad \varphi = \tan^{-1}\frac{\omega_{CR}(r)\omega_{dr}}{Q([\omega_{CR}(r)]^2 - \omega_{dr}^2)} \tag{6}$$

where A_0 is the amplitude in the resonance, $\omega_{CR}(r)=2\pi f_{CR}(r)$ is the circular resonance frequency of the cantilever in the contact that depends on the position r, and $\omega_{dr}=2\pi f_{dr}$ is the circular driving frequency, and Q is the quality factor of the cantilever in the contact. Using this formalism, we can now simulate the amplitude dependence of the CR-AFM A(r,f_{dr}) that was presented in figure 3(a) and compare it to the experimental data. The results of this simulation are presented in figure 6(a,b) and show an excellent agreement between the model and the experimental measurements. As one can see, at f_{dr} close to the frequency of contact resonance of the supported MLG $f_{CR\text{-}R}$ (65 kHz, figure 6(d)) all suspended areas have low response, whereas at the frequency below $f_{CR\text{-}R}$ (62 kHz, figure 6(c)) the resonance appears at the radius close to the rim – explaining the bright ring we observed in figure

2(g). Essentially, by comparing the resonance frequency of the supported and the suspended areas figure 6(e), the modelling presented in the figure 4, and calibrated cantilever stiffness, allows one to directly determine the ratio of MLG plate stiffness in this point to the cantilever stiffness k_s/k_c=231 resulting in the membrane stiffness in this point of 42.7±0.2 N m^{-1}. This figure also demonstrates that the amplitude in the supported area is higher than the one in the centre of the membrane at 66 kHz while becoming lower at excitation frequencies below 65 kHz cross-over frequency. It is useful to note that CR-AFM is well suited for mapping and quantitative measurements if stiffness of stiffer membranes that becomes valuable for smaller sub-um dimensions MEMS structures of 2D materials. By using real-time mapping of the resonance frequency at each point of the sample during scan (similar to approach used in the piezo-force microscopy [42]) and analysis above, it is possible to produce high precision stiffness maps allowing direct interpretation of the internal structure in the multilayered and heterostructured 2D materials observed in figure 6(c-e).

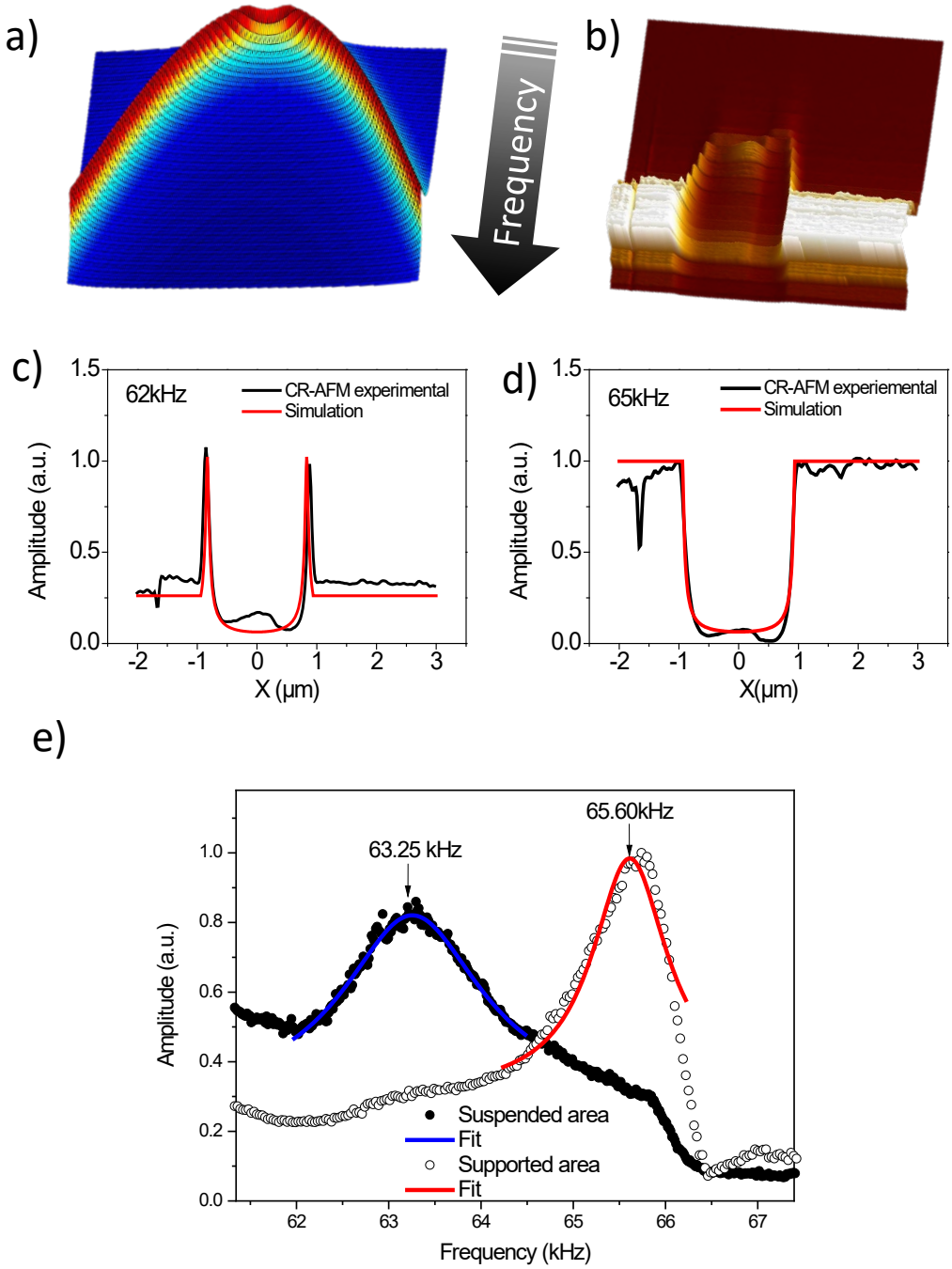

Figure 6 (a) Modeling of the amplitude response A(r,f_{dr}) of the CR-AFM as the function of the radius from the centre of the plate and the driving frequency f_{dr} for the 50 to 69 kHz frequency range, (b) experimental CR-AFM data of the A(r,f_{dr}) response for the same frequency range. (c, d) comparison of the simulated and measured one-dimensional profiles *A(r)* at the frequencies below and above contact resonance frequency for the solid contact. (e) Experimentally measured CR-AFM response in the area of the suspended MLG plate vs supported graphene, the frequency shift allows precisely determine the stiffness of the GR membrane in the particular point.

4. Conclusions

In summary, here we use the combination of the low and high frequency excitation dynamic force microscopy in the frequency range from 10 kHz to 5 MHz to investigate the details of the nanomechanical behaviour of the multilayer graphene plate suspended on the micromachined substrate. In particular, the high frequency UFM mapping allowed precise determination of the geometry of the suspended region even for the relatively thick plate, as well as observation of the faults at the MLG-substrate interface. By building an analytical model of the CR-AFM in application to the elastically deformed circular plate, we were able to perform absolute measurements of the mechanical stiffness of the 2D material nanostructure and to interpret the novel contrast phenomena specific to the 2D materials. The excellent agreement between the experimental and modelling data and high sensitivity of the method to the internal structure of MLG opens a great possibility to investigate multilayer heterostructures of 2D materials, and the 2D material –substrate interface.

Acknowledgements

Authors acknowledge the support of Manchester-Lancaster EPSRC Graphene NowNANO CDT, Lancaster University QTC and Lancaster Materials Science Institute. OVK acknowledges support of EPSRC grants EP/K023373/1 and EP/G06556X/1, EU Graphene Flagship, UKRI Faraday Institution NEXGENNA project and Paul Instrument Fund PI170026, c/o The Royal Society.

References

1. Wang, P., W. Gao, and R. Huang, *Entropic effects of thermal rippling on van der Waals interactions between monolayer graphene and a rigid substrate.* Journal of Applied Physics, 2016. **119**(7): p. 074305.
2. Walker, M.I., et al., *Free-standing graphene membranes on glass nanopores for ionic current measurements.* Applied Physics Letters, 2015. **106**(2): p. 023119.
3. Liu, Y. and X. Chen, *Mechanical properties of nanoporous graphene membrane.* Journal of Applied Physics, 2014. **115**(3): p. 034303.
4. Young, W.C. and R.G. Budynas, *Roark's formulas for stress and strain*. Vol. 7. 2002: McGraw-Hill New York.
5. Poot, M. and H.S.J. van der Zant, *Mechanical systems in the quantum regime.* Physics Reports-Review Section of Physics Letters, 2012. **511**(5): p. 273-335.
6. Zande, A.M.v.d., et al., *Large-Scale Arrays of Single-Layer Graphene Resonators.* Nano Letters, 2010. **10**(12): p. 4869-4873.
7. Poot, M. and H.S.J. van der Zant, *Nanomechanical properties of few-layer graphene membranes.* Applied Physics Letters, 2008. **92**(6).
8. Booth, T.J., et al., *Macroscopic graphene membranes and their extraordinary stiffness.* Nano Letters, 2008. **8**(8): p. 2442-2446.
9. Clark, N., A. Oikonomou, and A. Vijayaraghavan, *Ultrafast quantitative nanomechanical mapping of suspended graphene.* Physica Status Solidi B-Basic Solid State Physics, 2013. **250**(12): p. 2672-2677.

10. Khestanova, E., et al., *Universal shape and pressure inside bubbles appearing in van der Waals heterostructures.* Nature Communications, 2016. **7**: p. 12587.
11. Rollier, A.-S., et al. *Tensile stress determination in silicon nitride membrane by AFM characterization*. in *TRANSDUCERS, The 13th International Confercnce on Solid-State Sensors, Actuators and Microsystems 10.1109/SENSOR.2005.1496545*. 2005. Seoul, Korea.
12. Storch, I.R., et al., *Young's modulus and thermal expansion of tensioned graphene membranes.* Physical Review B, 2018. **98**(8): p. 085408.
13. Dinelli, F., et al., *Subsurface imaging of two-dimensional materials at the nanoscale.* Nanotechnology, 2017. **28**(8): p. 085706.
14. Tu, Q., et al., *Interfacial Mechanical Properties of Graphene on Self-Assembled Monolayers: Experiments and Simulations.* Acs Applied Materials & Interfaces, 2017. **9**(11): p. 10203-10213.
15. Mazzocco, R., et al., *Surface and interfacial interactions of multilayer graphitic structures with local environment.* Thin Solid Films, 2015. **585**(0): p. 31-39.
16. Ma, C., et al., *Depth-sensing using AFM contact-resonance imaging and spectroscopy at the nanoscale.* Journal of Applied Physics, 2019. **126**(12): p. 124302.
17. Yip, K., et al., *Investigating the detection limit of subsurface holes under graphite with atomic force acoustic microscopy.* Nanoscale, 2019. **11**(22): p. 10961-10967.
18. Ma, C., et al., *Detection of subsurface cavity structures using contact-resonance atomic force microscopy.* Journal of Applied Physics, 2017. **121**(15): p. 154301.
19. Wenting, W., Z. Wenhao, and C. Yuhang, *Enhancement of contact resonance AFM subsurface imaging by mass-attached cantilevers.* Journal of Physics D: Applied Physics, 2020.
20. Blake, P., et al., *Making graphene visible.* Applied Physics Letters, 2007. **91**(6): p. 063124-3.
21. Bosse, J.L., et al., *Physical mechanisms of megahertz vibrations and nonlinear detection in ultrasonic force and related microscopies.* Journal of Applied Physics, 2014. **115**(14): p. 144304.
22. Dinelli, F., et al., *Measurements of stiff-material compliance on the nanoscale using ultrasonic force microscopy.* Physical Review B, 2000. **61**(20): p. 13995-14006.
23. Robinson, B.J., N.D. Kay, and O.V. Kolosov, *Nanoscale Interfacial Interactions of Graphene with Polar and Nonpolar Liquids.* Langmuir, 2013. **29**(25): p. 7735-7742.
24. Sader, J.E., et al., *A virtual instrument to standardise the calibration of atomic force microscope cantilevers.* Review of Scientific Instruments, 2016. **87**(9): p. 093711.
25. Castellanos-Gomez, A., et al., *Mechanics of freely-suspended ultrathin layered materials.* Annalen Der Physik, 2015. **527**(1-2): p. 27-44.
26. Yamanaka, K. and S. Nakano, *Ultrasonic atomic force microscope with overtone excitation of cantilever.* Japanese Journal of Applied Physics Part 1-Regular Papers Short Notes & Review Papers, 1996. **35**(6B): p. 3787-3792.
27. Hirsekorn, S., U. Rabe, and W. Arnold, *Theoretical description of the transfer of vibrations from a sample to the cantilever of an atomic force microscope.* Nanotechnology, 1997. **8**(2): p. 57-66.
28. Wright, O.B. and N. Nishiguchi, *Vibrational dynamics of force microscopy: Effect of tip dimensions.* Applied Physics Letters, 1997. **71**(5): p. 626-628.
29. Rossing, T.D. and N.H. Fletcher, *Principles of Vibration and Sound*. 2nd ed. 2004: Springer. 330 p.
30. Sherchenkov, A., et al., *CRYSTALLIZATION MECHANISM AND KINETIC PARAMETERS IN Ge2Sb2Te5 THIN FILMS FOR THE PHASE CHANGE MEMORY APPLICATION.* Chalcogenide Letters, 2018. **15**(1): p. 45-54.
31. Dinelli, F., et al., *Ultrasound induced lubricity in microscopic contact.* Applied Physics Letters, 1997. **71**(9): p. 1177-1179.
32. Rabe, U. and W. Arnold, *Acoustic microscopy by atomic force microscopy.* Applied Physics Letters, 1994. **64**(12): p. 1493-1495.

33. Kay, N.D., et al., *Electromechanical Sensing of Substrate Charge Hidden under Atomic 2D Crystals.* Nano Letters, 2014. **14**(6): p. 3400.
34. Kolosov, O. and K. Yamanaka, *Nonlinear detection of ultrasonic vibrations in an atomic-force microscope.* Japanese Journal of Applied Physics Part 2-Letters, 1993. **32**(8A): p. L1095-L1098.
35. Yuya, P.A., D.C. Hurley, and J.A. Turner, *Contact-resonance atomic force microscopy for viscoelasticity.* Journal of Applied Physics, 2008. **104**(7): p. 074916.
36. Tetard, L., A. Passian, and T. Thundat, *New modes for subsurface atomic force microscopy through nanomechanical coupling.* Nature Nanotechnology, 2010. **5**(2): p. 105-109.
37. Liu, Z., et al., *Interlayer shear strength of single crystalline graphite.* Acta Mechanica Sinica, 2012. **28**(4): p. 978-982.
38. Reguzzoni, M., et al., *Friction by Shear Deformations in Multilayer Graphene.* The Journal of Physical Chemistry C, 2012. **116**(39): p. 21104-21108.
39. Zandiatashbar, A., et al., *Effect of defects on the intrinsic strength and stiffness of graphene.* Nature Communications, 2014. **5**(1): p. 3186.
40. Young, W.C., R.G. Budynas, and A.M. Sadegh, *Roark's formulas for stress and strain*. Vol. 7. 2002: McGraw-Hill New York.
41. Lee, C., et al., *Measurement of the elastic properties and intrinsic strength of monolayer graphene.* Science, 2008. **321**(5887): p. 385-388.
42. Jesse, S., P. Maksymovych, and S.V. Kalinin, *Rapid multidimensional data acquisition in scanning probe microscopy applied to local polarization dynamics and voltage dependent contact mechanics.* Applied Physics Letters, 2008. **93**(11).

Supplementary Materials.

Mapping nanoscale dynamic properties of suspended and supported multi-layer graphene membranes via contact resonance and ultrasonic scanning probe microscopies

Marta Mucientes[1*], Robert McNair[2], Adrian Peasey[2], Shouqi Shao[2], Joshua Wengraf[2], Kunal Lulla[1], Benjamin J. Robinson[1,3] and Oleg Kolosov[1,3**].

[1]Physics Department, Lancaster University, Lancaster LA1 4YB, UK

[2]Graphene NowNANO CDT, School of Physics and Astronomy, The University of Manchester, Manchester, M13 9PL, UK

[3]Materials Science Institute, Lancaster University, Lancaster LA1 4YW, UK

Email: *m.sanjuanmucientes@lancaster.ac.uk, **o.kolosov@lancaster.ac.uk,

SM1. Substrate preparation.

The substrates were first cleaned by sequential sonication in acetone and isopropyl alcohol (10 min each) followed by an O_2 (40 sccm; 200 mTorr, 50W) plasma in the reactive ion etching (RIE) (Oxford Instruments PlasmaPro® NGP80) during 3 minutes to remove any organic contamination from the surface. To pattern the substrates, the negative photo-resist S1813 was spin-coated at 4000 rpm for 45 sec and baked at 115° for 2 min. The resist was exposed to the UV light during 2.7 seconds with hard contact in the MJB4 Mask Aligner (SUSS MicroTec, Germany) to transfer the pattern. Post-exposure, the samples were baked for 1 min at 115° and developed in MFCD26 for 90 seconds. The next step was 7.5 min RIE, with a gas mixture of CHF_3 (25sccm) and Ar (5 sccm), at a pressure of 30mTorr in the chamber and a RF power of 150 W. Finally, the wafers were cleaned to remove all the resist residue with the O_2 plasma during 3 minutes and in the ultrasonic bath with Acetone and IPA during 5 minutes. Figure 1 shows the resulting hole.

SM2. Resonance frequencies of clamped plate and membrane.

To find the fundamental resonance frequency f_{plate} of a clampled plate of thickness t and radius R, we used the equation [1]

$$f_{plate} = \frac{10.21}{4\pi}\sqrt{\frac{E_s}{3\rho_s(1-{\nu_s}^2)}}\frac{t}{R^2} \qquad (1)$$

Nevertheless, for the determination of the fundamental resonance of a membrane $f_{membrane}$ under pre-tension T, the equation used was:

$$f_{membrane} = \frac{2.4048}{2\pi R}\sqrt{\frac{T}{\rho_s t}} \quad (2)$$

In both cases, the physical properties of the material are density ρ_s, Young's Modulus E_s, and the Poisson's ratio v_s.

SM3. Calculating the resonance of the cantilever in contact with the spring.

The motion of the cantilever-sample can be modeled as a cantilever supported in the free end by a spring, with respective k_c and k_s cantilever and sample stiffness. The equation of the deflection of a cantilever of thickness *h* is given as:

$$\frac{\partial^2 z}{\partial t^2} + \frac{E_c h^2}{12\rho_c}\frac{\partial^4 z}{\partial x^4} = 0 \quad (3)$$

where *x-z* are the coordinates, E_s and ρ_s are respectively the Young's modulus and density of the cantilever material.

In the literature, they assumed that the solution of the equation (3) takes the form

$$z = C\sin(\omega t + \delta)\Phi(x) \quad (4)$$

with

$$\begin{aligned}\Phi(x) = (\sin\alpha + \sinh\alpha)\left(\cos\frac{\alpha}{L}x - \cosh\frac{\alpha}{L}x\right) \\ + (\cos\alpha + \cosh\alpha)\left(\sin\frac{\alpha}{L}x - \sinh\frac{\alpha}{L}x\right)\end{aligned} \quad (5)$$

where ω is the angular frequency, *L* is the length of the cantilever and the constant

$$\alpha = \left(\frac{12\rho_c\omega^2 L^4}{E_c h^2}\right)^{\frac{1}{4}} \quad (6)$$

relates the cantilever parameters with the resonance frequency. This constant was obtained from the boundary conditions. Furthermore, considering that the sample behaves such as linear spring, the motion equation can be written as

$$\frac{k_c}{3k_s}\alpha^3 P(\alpha) = Q(\alpha) \quad (7)$$

where *P(α)* and *Q(α)* are defined as

$$P(\alpha) = 1 + \cos\alpha\cosh\alpha \quad (8)$$

$$Q(\alpha) = \cos\alpha\sinh\alpha - \sin\alpha\cosh\alpha \quad (9)$$

Solving numerically the equations 8 and 9, for the boundary conditions below of the relation between the stiffness of the sample and the cantilever, we calculated the value of α = 3.92.

$$k_s \ll k_c \Rightarrow P(\alpha) \to 0 \quad (10)$$

$$k_c \ll k_s \Rightarrow Q(\alpha) \to 0 \quad (11)$$

In the first case, the ratio between the stiffness of the sample and the cantilever corresponds experimentally with free cantilever, $k_s \to 0$, with resonance frequency: $f_{free\text{-}cantilever}$ = 13.8 kHz. And

the second one is corresponding with the probing point in the supported multilayer graphene (MLG) $k_s \rightarrow \infty$, $f_{substrate}$ = 64.6 kHz.

Solving numerically the equations 8 and 9, for the boundary conditions below of the relation between the stiffness of the sample and the cantilever, we calculated the value of α = 3.92.

SM4. Estimating shear stresses in the multilayer graphene (MLG) .

In order to estimate the possibility of interlayer sliding in MLG that may influence the measurement results, we have calculated the maximal local shear stresses in the membrane using final element analysis (FEA) software (COMSOL, solid mechanics module) under the typical forces applied by the AFM tip.

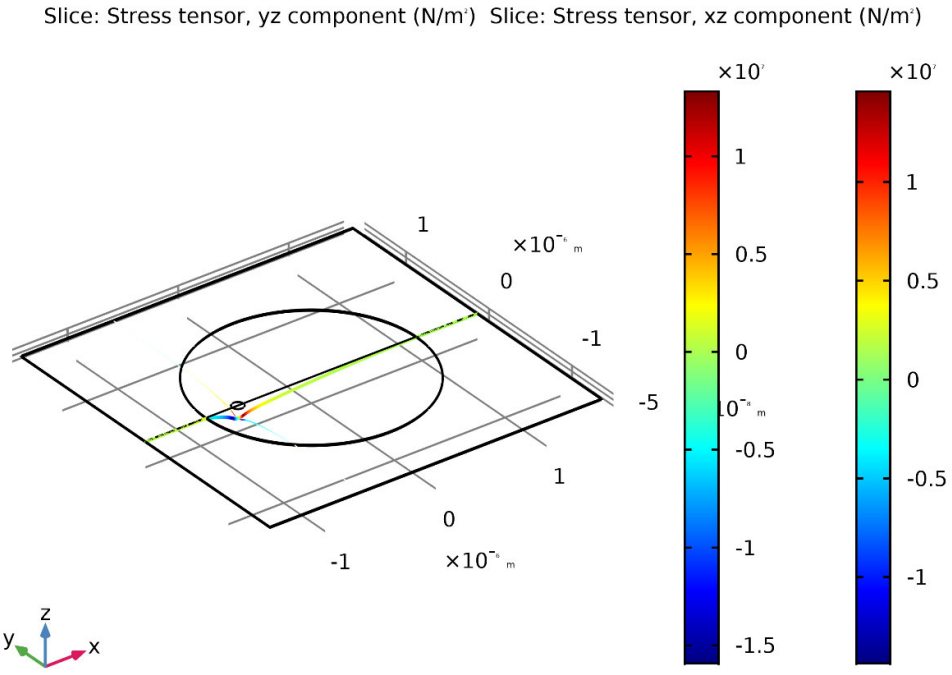

Figure S1. FEA modelling of the stresses in the 10 nm GR membrane on the 1.9 um opening under 50 nN force applied to the AFM tip.

We found that the maximal shear stress was below 1.5×10^{7} N m^{-2} that is an order of magnitude smaller than typical shear strength between GR layers required for the sliding reported to be on the order of $1.5\text{-}1.8\times10^{8}$ N m^{-2} [2, 3].

REFERENCES

1. Rossing, T.D. and N.H. Fletcher, *Principles of Vibration and Sound*. 2nd ed. 2004: Springer. 330 p.
2. Liu, Z., et al., *Interlayer shear strength of single crystalline graphite.* Acta Mechanica Sinica, 2012. **28**(4): p. 978-982.
3. Reguzzoni, M., et al., *Friction by Shear Deformations in Multilayer Graphene.* The Journal of Physical Chemistry C, 2012. **116**(39): p. 21104-21108.